Research paper

Geochemical characterization and methane adsorption capacity of overmature organic-rich Lower Cambrian shales in northeast Guizhou region, southwest China

Tengfei Li [a, b], Hui Tian [a, *], Xianming Xiao [a], Peng Cheng [a], Qin Zhou [a], Qiang Wei [a, b]

[a] State Key Laboratory of Organic Geochemistry, Guangzhou Institute of Geochemistry, Chinese Academy of Sciences, Guangzhou 510640, China
[b] University of Chinese Academy of Science, Beijing 100049, China

ABSTRACT

The Niutitang Shale (Lower Cambrian) is another set of organic-rich shale in addition to the Lower Silurian Longmaxi Shale in southwest China. In this study, methane adsorption capacities of both whole rock and organic matter were investigated based on adsorption isotherms measured at various temperatures (40–120 °C) and pressures (up to 35.0 MPa) for eleven Niutitang Shale samples collected from northeast Guizhou Province. The investigated samples cover a wide range of TOC contents, varying from 1.8 to 11.3%, with an average equivalent vitrinite reflectance (EqVRo) value of approximately 4.0%; their BET specific surface areas and micropore volumes range from 11.1 to 26.2 m^2/g rock and between 4.3 and 11.2 cm^3/kg rock, respectively, both of which are positively correlated to TOC content. Model-fitted methane maximum absolute adsorption capacities (n_∞) range from 1.80 to 5.85 cm^3/g rock at 60 °C and are found to largely increase with increasing TOC; this suggests that the TOC control on methane adsorption capacity obtained by other authors for other shales with relative low thermal maturity levels may be extended to a very high thermal maturity level, e.g., EqVRo≈4.0%. The methane adsorption capacity of organic matter (OM) in our shale samples, however, is somehow reduced as compared to the Lower Silurian Longmaxi Shale and other shales that display EqVRo values smaller than 3.0%, indicating thermal maturity may adversely affect methane adsorption capacity of shales when it evolves to be EqVRo≈4.0%. Nevertheless, this reduction in adsorption capacity may be compensated by the very enrichment of OM in the Niutitang Shale. In addition, a higher thermal maturity level results in a lower Langmuir pressure value, which makes it more difficult for methane desorption at reservoirs conditions. The temperature dependency of adsorption parameters was also investigated, which could be used to predict the changes of methane adsorption with burial depth under geological conditions beyond experimental temperature and pressure ranges.

© 2017 Elsevier Ltd. All rights reserved.

1. Introduction

One feature of unconventional shale gas reservoirs that distinguishes them from conventional gas reservoirs is that they can trap gas in both free and adsorption phases (Curtis, 2002). Shale gas systems may comprise 20–85% of adsorbed gas, depending on their organic/inorganic composition, thermal maturity level, moisture content, temperature and pressure conditions (Curtis, 2002; Jarvie, 2012). Early studies have illustrated that total organic carbon (TOC) content may be considered as to be a key control of shale gas content, and positive correlations were also observed between TOC and adsorbed gas capacity for many shales (Chalmers and Bustin, 2007; Ross and Bustin, 2009; Nie et al., 2011; Weniger et al., 2010; Hao et al., 2013; Gasparik et al., 2014a; Tian et al., 2016). Clay minerals also provide some sites for methane adsorption when they are free of moisture (Ji et al., 2012; Jin and Firoozabadi, 2014); otherwise, methane adsorption may occur mostly on the surface sites of organic matter (OM) that are more hydrophobic than clay minerals in geological conditions (Chalmers and Bustin, 2007, 2008; Wang et al., 2009).

Thermal maturity has also been reported to affect the sorption capacity of shales but there is no agreement on such effect. Ross and

---

Bustin (2009) suggests that thermally immature shales display lower methane adsorption capacities than thermally mature shales because the latter host more OM micropores (<2 nm in diameter) that are believed to serve as the main adsorption sites in shales (Rexer et al., 2014). However, other authors suggest that thermal maturity has only a trivial effect on the adsorption capacity of shales (Gasparik et al., 2012; Zhang et al., 2012) or even adversely affects their adsorption capacity (Yang et al., 2015). More interestingly, Gasparik et al. (2014a) reported an enhanced adsorption capacity of shales on TOC basis (i.e., the adsorption capacity of a shale sample is normalized to TOC content) within thermal maturation stages varying from immature to a Ro value of 1.9% but a decreasing trend beyond this thermal maturity range, though the decreasing trend is only constrained by few samples. In addition, thermal maturity also has an effect on the shape of methane adsorption isotherm, which can be manifested by the decreasing trend of Langmuir pressure with increasing thermal maturation at similar experimental temperatures (Zhang et al., 2012; Gasparik et al., 2014a). The Langmuir pressure refers to as a parameter that describes the capacity of methane desorption from a shale, a higher value indicating a stronger capacity to desorb, and therefore it is as crucial as adsorption capacity regarding shale gas production (Heller and Zoback, 2014).

The adsorption capacity of a shale sample is usually determined experimentally at a desired range of temperature and pressure. The measured adsorption isotherms is technically termed excess adsorption (Krooss et al., 2002) and can be fitted with various models (Mohammad et al., 2012; Rexer et al., 2013). With fitted adsorption parameters, the changes of methane adsorption with burial depth can be reconstructed for shales in subsurface (Bruns et al., 2016 and references therein). For excess adsorption isotherms that display no maxima, it is difficult, if not impossible, to determine their adsorption parameters unambiguously since measured isotherms can be satisfactorily fitted in all cases (Gensterblum et al., 2013). Therefore, excess adsorption isotherms are recommended to be obtained at pressures as high as possible to eliminate this ambiguity (Gasparik et al., 2014a, 2015). In addition, methane adsorption on shales is an exothermic process (Sircar, 1992), and therefore reduced adsorption capacity but enhanced Langmuir pressure are expected at elevated temperatures (Rexer et al., 2013; Tian et al., 2016). Thus, information on methane adsorption capacity at temperatures greater than the present reservoirs temperature is also required to investigate the evolution of shale gas content through geological time because most of shallow-buried gas shales today ever reached a greater burial depth and suffered a more severe thermal stress (Bruns et al., 2016). With adsorption isotherms measured at various temperatures, the temperature dependency of gas adsorption parameters such as the maximum gas adsorption potential at infinite pressure and density of adsorbed gas, can be obtained and hence may be extrapolated to
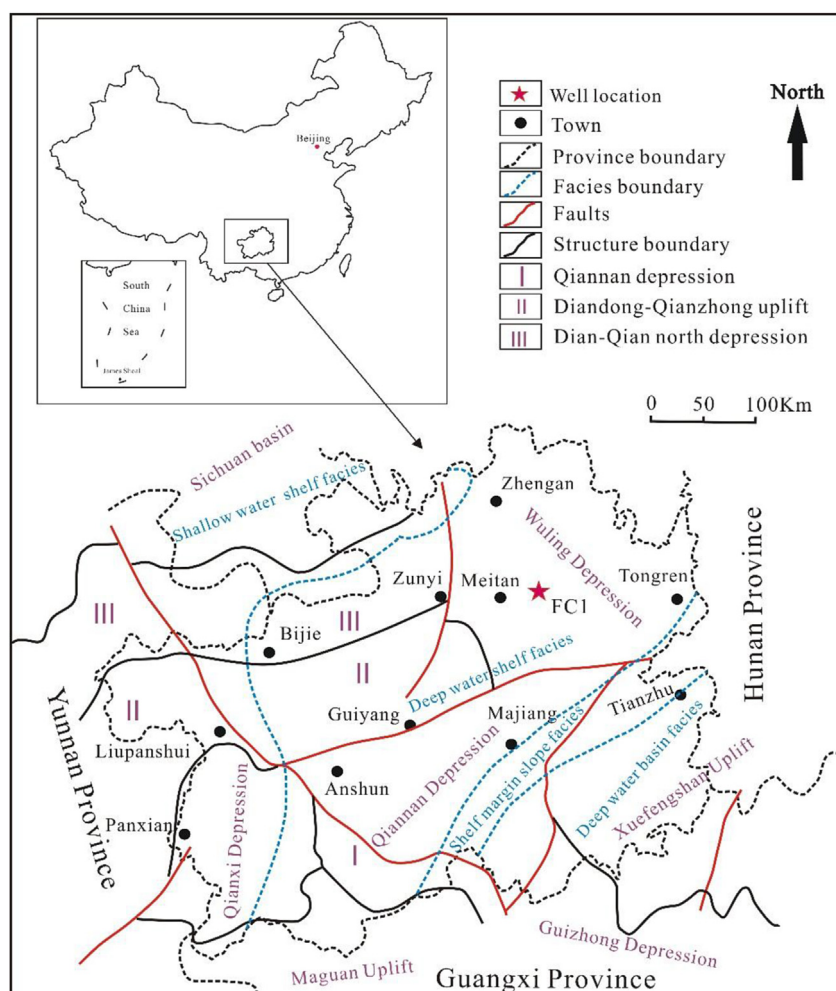

Fig. 1. Schematic map showing structural units, depositional environments and sampling location (modified from Tian et al., 2006; Liu et al., 2017).
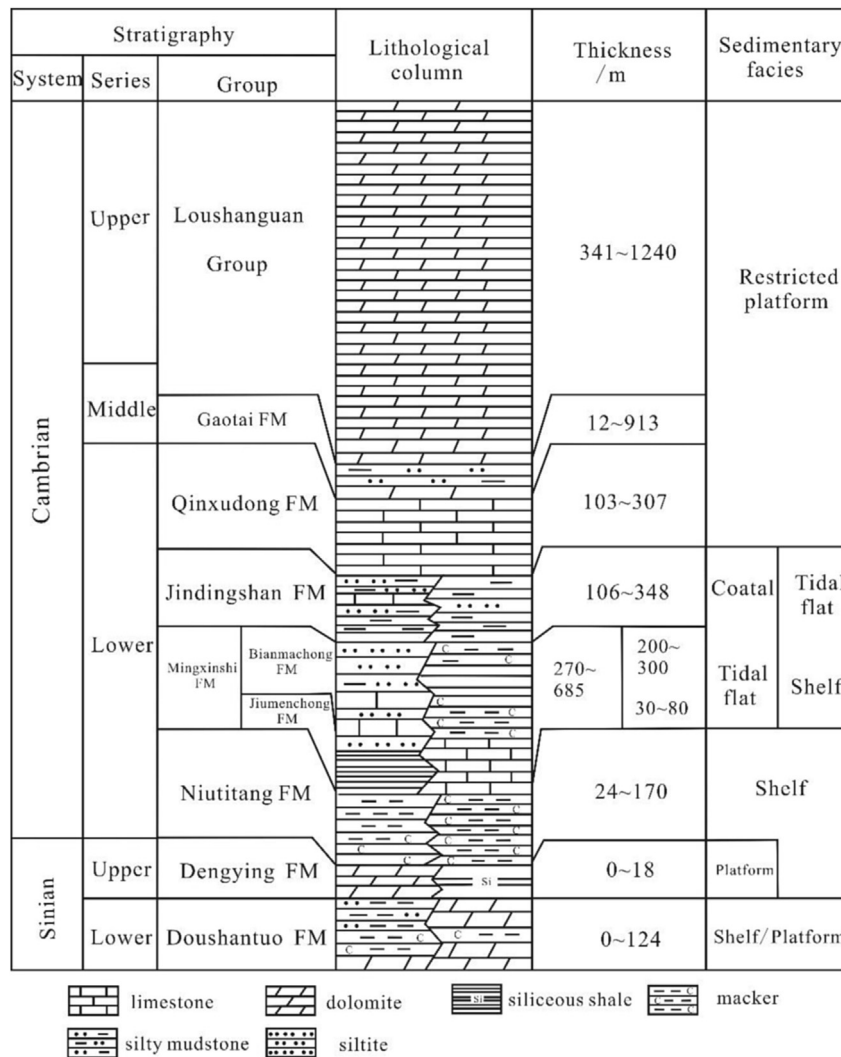
Fig. 2. A brief stratigraphic column of northeast Guizhou Province (modified from Wang et al., 2016; Leng et al., 2016).

Table 1
TOC, mean bitumen reflectance and mineralogical composition for the eleven Lower Cambrian shale samples.

Sample	Age	Depth	TOC	[a]Pyrobitumen reflectance	XRD mineralogical composition (%)						S_{BET}	[b]V_{total}	[c]V_{mic}
		(m)	(%)	(%)	Quartz	Feldspar	Carbonates	Pyrite	Total clay	Apatite	(m^2/g rock)	cm^3/kg rock	cm^3/kg
FC-37	ϵ_1	2449	1.8	3.5–4.7(4.1)	27.3	26.5	6.4	3.6	34.4	n.d.	11.1	8.9	4.4
FC-38	ϵ_1	2449	2.5	n.d.	28.9	33.8	5.2	3.3	26.3	n.d.	11.1	9.2	4.3
FC-45	ϵ_1	2462	6.1	n.d.	34.8	36.7	4.7	3.9	13.7	n.d.	16.4	11.4	7.2
FC-47	ϵ_1	2466	3.5	n.d.	48.6	18.8	11.9	4.5	12.6	n.d.	12.1	8.9	5.7
FC-49	ϵ_1	2469	4.7	n.d.	51.9	17.6	10.7	4.6	10.5	n.d.	13.3	9.2	8.3
FC-53	ϵ_1	2475	10.7	3.2–4.5(3.8)	52.3	9.1	3.6	3.3	21.0	n.d.	26.2	17.5	11.2
FC-55	ϵ_1	2477	8.6	3.7–4.3(3.9)	43.8	19.8	6.0	4.8	17.0	n.d.	19.9	13.2	9.4
FC-59	ϵ_1	2491	9.2	n.d.	45.1	26.2	n.d.	4.4	15.2	n.d.	18.3	14.7	9.4
FC-62	ϵ_1	2498	6.8	3.3–4.0(3.7)	30.3	35.5	n.d.	3.2	24.3	n.d.	15.2	14.1	7.2
FC-66	ϵ_1	2521	7.3	3.5–4.5(3.9)	44.2	18.7	n.d.	3.2	26.6	n.d.	18.4	14.9	8.2
FC-72	ϵ_1	2538	11.3	n.d.	38.1	17.4	n.d.	5.2	14.5	13.6	23.6	18.6	11.2

n.d. indicates no data.
  [a] Mean pyrobitumen reflectance is reported in brackets.
  [b] Total pore volume determined by the adsorbed nitrogen at 77.4 K at a relative pressure of 0.995.
  [c] Micropore volume determined by the DR equation with CO_2 adsorption at 273.15 K.

geological conditions with more confidence than before (Rexer et al., 2013).

Over past years, a wealthy of studies have been conducted on the Lower Silurian shales in southwest China with respect to their geochemistry, pore structure and gas storage capacity (Chen et al., 2011; Tian et al., 2013; Wang et al., 2013b; Tan et al., 2014a, b; Dai
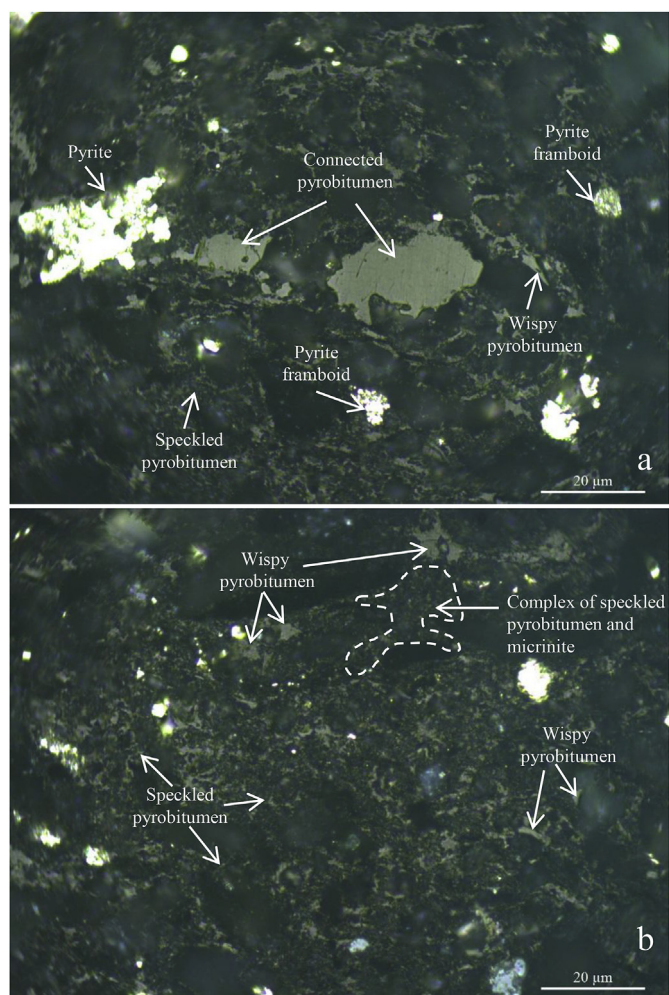
Fig. 3. Whole rock-based microphotographs of pyrobitumen and micrinite macerals. According to the size of pyrobitume grains (Cardott et al., 2015), they are described to be connected (>5 μm), wispy (2–5 μm) and speckled (<1–2 μm) (a, sample FC-62); micrinite usually occurs with speckled pyrobitumen particles, forming a maceral complex (b, sample FC-66).

et al., 2016). The Lower Cambrian shales — another important set of black shales in southwest China, however, are only still poorly documented with some studies on their geochemistry and pore structures (Han et al., 2013; Tian et al., 2015; Yang et al., 2016 and references therein) and some studies with respect to methane adsorption and gas storage capacity at relatively low temperature and pressure ranges for outcrop and/or shallow-well samples (Tan et al., 2014b; Chen et al., 2015; Ma et al., 2015; Sun et al., 2015; Li et al., 2016a). The Lower Cambrian shales are more organic-rich but display higher thermal maturity levels than the Lower Silurian shales, with EqVRo values mostly greater than 3.0% (Nie et al., 2011; Hao et al., 2013; Tan et al., 2014b). Early studies have shown that porosities of Lower Cambrian shales in Sichuan Basin are generally smaller than those of Lower Silurian shales with similar TOC contents because the former might have been more severely compacted and thermally matured (Wang et al., 2013a; Tian et al., 2015). However, it is still not clear whether the methane adsorption capacity is also correspondingly reduced due to severe compaction and thermal maturation.

In this study, eleven Lower Cambrian shale samples were collected from a well that was drilled in 2015 in northeast Guizhou Province, a new promising shale gas area outside Sichuan Basin

(Han et al., 2013; Wu et al., 2017). Geochemical analysis and methane adsorption experiments at various temperatures (40–120 °C) and pressures (approximately 0.2–35 MPa) were performed to investigate their methane adsorption capacity and main controls, which would help understand thermal maturity effect on methane adsorption capacity of shales at overmature stages, and hence the shale gas potential of Lower Cambrian shales in China.

2. Geological setting

The study area sits in the northeast part of Guizhou Province and is tectonically located in the Wuling Depression that is connected with the Sichuan Basin in northwest and bounded by the Xue-fengshan Uplift and Diandong-Qianzhong Uplift in southeast and southwest, respectively (Fig. 1). As part of an active continental margin during Mesoproterozoic (Wang et al., 2012), the study area evolved to be a continental rift basin during Early to Middle Neo-proterozoic, receiving varying thickness of volcanic and clastic sediments that partly comprise the basement rocks for the Early Paleozoic marine sedimentary basin (Bai et al., 2015). During late Neoproterozoic to Early Ordovician, the study area became to be part of passive continental margin and accumulated a series of carbonate and clastic sediments with water deepening southeast-ward and carbonate content increasing northwestward (Wang et al., 2012; Bai et al., 2015). With the rapid marine transgression during the very early Cambrian, the organic-rich Niutitang Shale was formed in a deep water shelf environment, unconformably overlying the Upper Ediacaran Dengying dolomites deposited in a sedimentary environment of shallow water carbonate platform (Zhou et al., 2012; Leng et al., 2016, Fig. 2). The organic-rich Niu-titang Shale is stably and widely distributed, with thickness varying from 80 to 110 m in northeast Guizhou Province (Leng et al., 2016; Liu et al., 2017). Following the rapid marine transgression during the very early Cambrian (e.g., Terreneuvian Epoch), the study area entered a stage of slow marine regression, which transformed its depositional environments from deep water continental shelf to transitional shallow water continental shelf and tidal zone, and eventually to a restricted carbonate platform in which a series of dolomite sequences formed (Fig. 2; Leng et al., 2016; Wu et al., 2017).

Beginning from Middle Ordovician, the study area entered a stage of foreland basin; it continued to late Silurian and accom-modated a series of carbonate and clastic sequences formed under various depositional environments (Bai et al., 2015). For example, the Wufeng-Longmaxi shales, another set of organic-rich shales in South China (Zou et al., 2010), were deposited in a sedimentary environment of deep water continental shelf with the rapid rising of global third-order sea level during Late Ordovician to Early Silurian (Su et al., 2007). During Devonian to Middle Triassic the study area subsided again and evolved to the stage of epiconti-nental basin until the Indosinian Orogeny at late Triassic that transformed it to a compressional foreland basin or an intra-continental basin in which clastic sequences predominate (Liu et al., 2012; Bai et al., 2015). With the early Yanshanian Orogeny at the end of Middle Jurassic, sedimentary process ceased, and most of the Upper Paleozoic to Mesozoic strata in northeast Guizhou region were eroded during late Yanshanian through Himalayan orogenies (Zhou et al., 2012; Leng et al., 2016). At the same time, the Yanshanian and Himalayan orogenies also finally established the tectonic pattern today, forming a lot of folds and faults largely striking NNE, NE and NS in the study area (Liu et al., 2012; Wu et al., 2017).
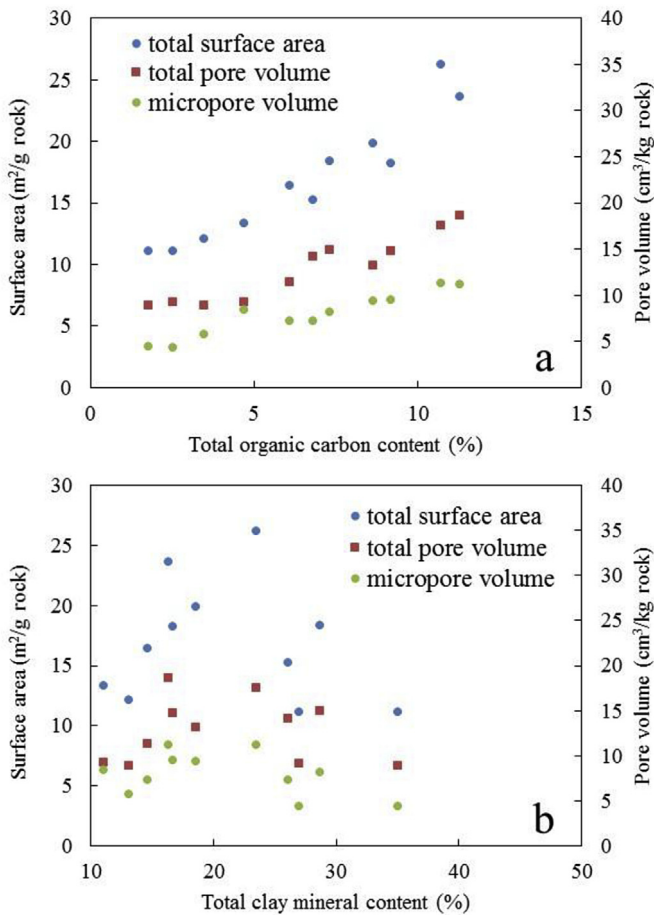
Fig. 4. Plots showing relationships of total surface area(S_{BET}), total pore volume (V_{total}) and micropore volume (V_{mic}) with TOC (a) and total clay mineral contents (b) for our eleven samples.

3. Samples and methods

3.1. Samples

Eleven gray to black shale cores were sampled from the 2449−2538 m interval (Table 1) of the Fengcan1 (FC1) well that was drilled in 2015 in northeast Guizhou Province (Fig. 1).

3.2. Geochemical and petrological analysis

Samples were ground and fully treated with hydrochloric acid before they are subject to total organic carbon (TOC) analysis with a carbon/sulfur analyzer. The measurement of pyrobitumen reflectance was conducted under oil immersion on polished whole rock blocks to investigate thermal maturity levels of the samples due to the lack of vitrinite in them (Tian et al., 2013). The mineralogical composition was analyzed with a Bruker D8 ADVANCE X-ray diffractometer on whole rock basis after the samples were ground to grains of smaller than 200 mesh (<70 μm in size). The working volt and current are 40 kV and 30 mA, respectively, with a scanning range of 3−85° (2θ) at a rate of 4°/min. The semi-quantitative analysis of mineral composition follows the method mentioned by Chalmers and Bustin (2008).
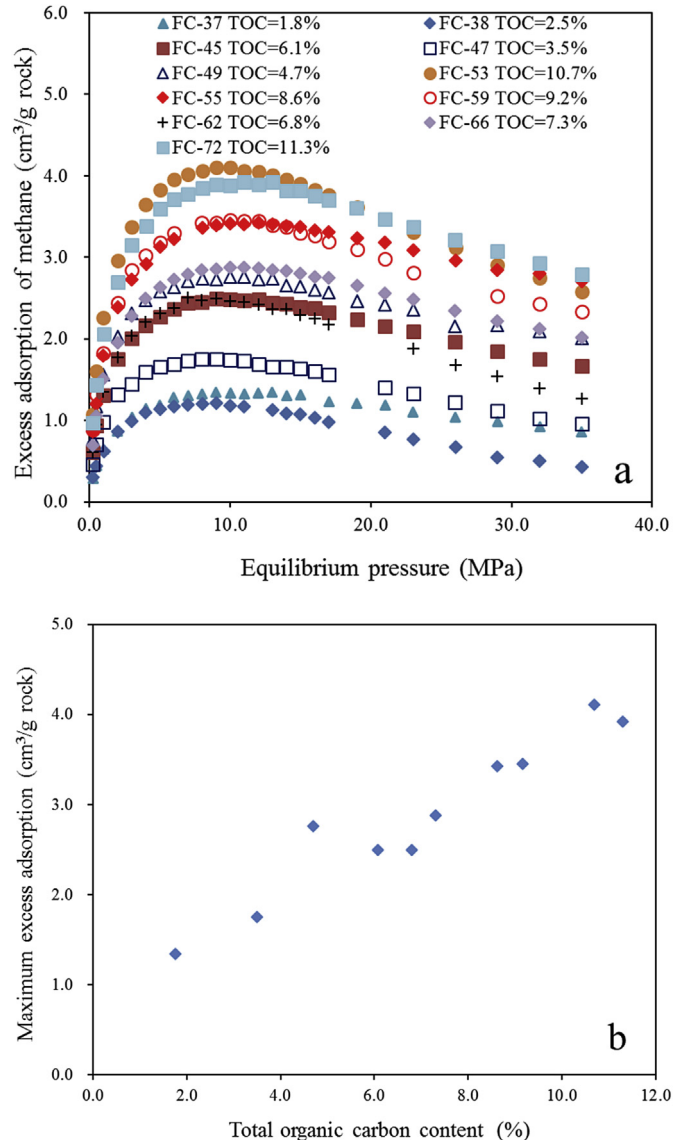

Fig. 5. Methane excess adsorption isotherms (a) and maxima of excess adsorption (b) at 60 °C for the eleven samples.

3.3. N_2 and CO_2 gas adsorption

Both N_2 and CO_2 adsorption experiments were performed on 1−2 g sample grains of approximately 20−50 mesh (300−750 μm in diameter) using a Micromeritics ASAP 2020^M apparatus. The nitrogen adsorption was conducted at 77.4 K, with a relative pressure (p/p$_0$) range of 0.0009−0.995 and an equilibrium time of 30 s; the experimental temperature was 273.15 K (0 °C) for CO_2 adsorption, with relative pressures (p/p$_0$) ranging from 0.00001 to 0.032 and an equilibrium time of 30 s.

The apparent specific surface area (S_{BET}) was determined with the BET model based on N_2 adsorption data. An appropriate relative pressure range was selected with the method of Rouquerol et al. (2007) that ensures both a positive BET C value and a high fitting quality with the coefficient of determination (R^2) greater than 0.9999 (Tian et al., 2015). In terms of the quantity of nitrogen adsorbed at 77.4 K at p/p$_o$ = 0.995, the total pore volume (V_{total}) of a shale sample was estimated; the micropore (<2 nm in diameter) volume (V_{mic}) was determined with the Dubinin−Radushkevich

Table 2
Methane adsorption parameters fitted with both 3-parameter SDR and Langmuir models based on excess adsorption isotherms measured at 60 °C with pressures up to 35 MPa.

Sample	TOC (%)	3-parameter SDR model			3-parameter Langmuir model		
		n_∞ (cm^3/g rock)	D (mol^2·kJ^{-2})	Pads (mg/cm3)	n_∞ (cm^3/g rock)	K_L (MPa^{-1})	ρ_{ads} (mg/cm^3)
FC-37	1.8	1.97	0.00841	364	2.01	0.40	377
FC-38	2.5	1.80	0.00938	264	1.90	0.45	266
FC-45	6.1	3.56	0.00730	383	3.60	0.47	397
FC-47	3.5	2.56	0.00731	328	2.52	0.62	344
FC-49	4.7	3.83	0.00621	419	3.62	0.68	480
FC-53	10.7	5.84	0.00708	372	5.85	0.54	386
FC-55	8.6	4.83	0.00663	465	4.55	0.58	541
FC-59	9.2	5.23	0.00974	373	4.69	0.60	457
FC-62	6.8	3.61	0.00790	313	3.75	0.48	316
FC-66	7.3	4.11	0.00718	406	4.16	0.45	420
FC-72	11.3	5.56	0.00700	415	5.44	0.51	444

(DR) equation based on the CO_2 adsorption isotherms (Gregg and Sing, 1982).

3.4. High-pressure methane adsorption

3.4.1. Measurement of excess adsorption with methane

Measurement of methane excess adsorption isotherms was conducted under various temperatures (40–120 °C) at pressures up to 35.0 MPa using a gas adsorption setup that is produced by Rubotherm GmbH, Germany (ISOSORP-HP Static II) and has a weighing precision of 0.01 mg (Pan et al., 2016). The same grain fractions (approximately 5–6 g) as used in N_2 and CO_2 adsorption experiments were utilized for methane adsorption measurement. Before methane adsorption, samples were outgassed and dried in the sample chamber for 12 h at 110 °C under a vacuum condition (approximately 0.01 atmospheric pressure) to remove the moisture in the samples. The equilibrium time for methane adsorption was set to be 2 h. The details of excess adsorption measurement using such type of setup can be found in literature (De Weireld et al., 1999; Ottiger et al., 2008 and references therein). Briefly, the measurable excess adsorption amount (n_{excess}) is calculated at desired temperature and pressure by the following equation (Ottiger et al., 2008):

$$n_{excess} = m_i - m_0 + \rho_g V_0 \tag{1}$$

where m_i is the weighted quantity of both the sample and sample container at the ith pair of temperature (T) and equilibrium pressure (P); m_0 is the weighted quantity of both the sample and sample container in vacuum condition before methane adsorption; ρ_g denotes the bulk density of methane that can be directly measured through a calibrated titanium sinker during experiment; V_0 is the total void volume of both sample and sample container and was determined with helium expansion at the same temperatures for methane adsorption (Gasparik et al., 2015). One of error sources for excess adsorption is derived from the error in void volume measurement (Gasparik et al., 2012, 2014b). As illustrated in Eq. (1), the error caused by void volume uncertainty is expected to increases with pressure for an isotherm at a given temperature because the bulk density of methane becomes larger and larger (Gasparik et al., 2014b); such error was estimated to be about 0.1–0.2 mg/g rock (0.14–0.28 cm^3/g rock at standard temperature and pressure (STP) conditions, i.e., 0 °C and 0.1 MPa) at 35 MPa and 40 °C for our samples, and this error range is comparable with that reported by Gasparik et al. (2012; 2014b).

3.4.2. Methane excess adsorption models

Methane excess adsorption isotherms were described with either 3-parameter Langmuir model (Eq. (2); Gasparik et al., 2014a) or 3-parameter SDR model (Eq. (3); Tian et al., 2016).

$$n_{excess} = n_\infty \cdot \frac{K_L \cdot P}{1 + K_L \cdot P} \cdot \left(1 - \frac{\rho_g}{\rho_{ads}}\right) \tag{2}$$

$$n_{excess} = n_\infty \cdot exp\left\{-D \cdot \left[ln\left(\frac{\rho_{ads}}{\rho_g}\right) \cdot R \cdot T_K\right]^2\right\} \cdot \left(1 - \frac{\rho_g}{\rho_{ads}}\right) \tag{3}$$

Where n_∞ denotes the maximum of methane absolute adsorption; K_L is Langmuir constant; P is equilibrium pressure; ρ_{ads} denotes the adsorbed phase methane density; D represents a pore structure parameter; R denotes the universal gas constant; T_K is Kelvin temperature. Based on measured methane excess adsorption isotherms, the unknown parameters in Eqs. (2) and (3), i.e. n_∞, K_L, D, and ρ_{ads} were optimized using the method mentioned in literature (Rexer et al., 2013). During data fitting, all parameters except for D are assumed to be temperature dependent (Rexer et al., 2013; Tian et al., 2016).

3.5. Thermodynamics of methane adsorption

For a constant absolute adsorption amount (n), the required equilibrium pressure (P) depends on adsorption temperature (T_K) and their relationship can be manifested by Eq. (4) that consists of isosteric heat (Q_{st}), standard entropy (ΔS^0) and the universal gas constant (R) (Myers and Monson, 2002). According to Eq. (4), Q_{st} and ΔS^0 were respectively determined from the slope and intercept values of regression line on the plot of ln(P) against $1/T_K$ (Zhang et al., 2012). Note that the term $ln(0.1)$ in Eq. (4) is used for correcting the ΔS^0 to the standard atmospheric pressure (0.1 MPa) (Hu et al., 2015).

$$ln(P)_n = -\frac{Q_{st}}{R \cdot T_K} + \left(\frac{R \cdot ln(0.1) - \Delta S^0}{R}\right) \tag{4}$$

4. Results

4.1. Geochemical and petrological character

The eleven samples studied here display a TOC range of 1.8–11.3% (Table 1). The main macerals identified with optical microscopy include pyrobitumen and micrinite (Fig. 3). While pyrobitumen is a product of oil cracking in source rocks (Pepper and Dodd, 1995), the micrinite is considered as to be the residual kerogen that is originally composed of amorphous organic matter
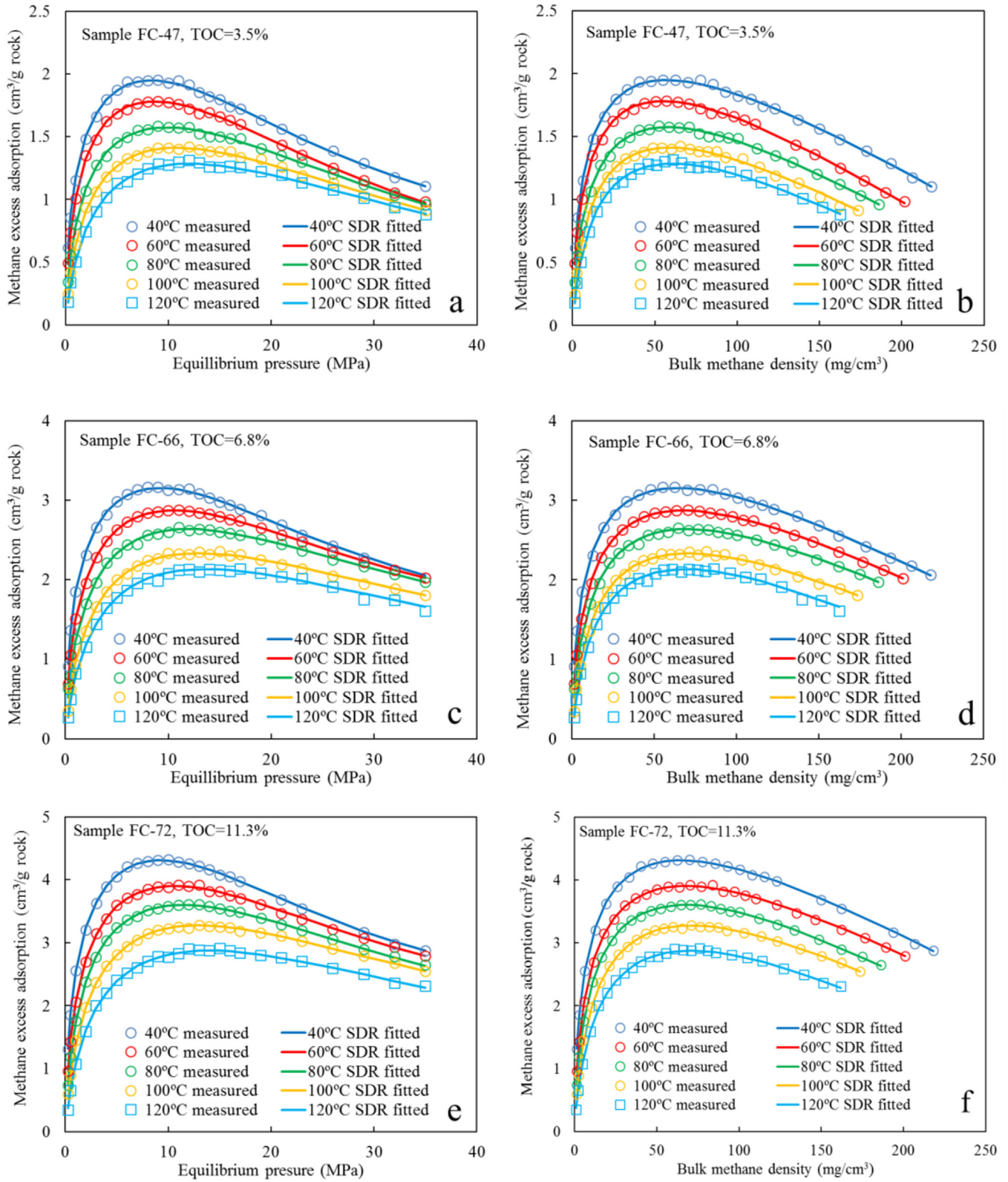
Fig. 6. Plots of measured and 3-parameter SDR model fitted excess adsorption isotherms against equilibrium pressure (a, c, e) and bulk methane density (b, d, f) at various temperatures for the three selected samples.

Table 3
Fitted methane adsorption parameters using both 3-parameter SDR and Langmuir models for the three selected samples at temperatures ranging from 40 to 120 °C.

Sample	Temp. (°C)	3-parameter SDR model			3-parameter Langmuir model		
		n_∞ (cm³/g rock)	D (mol²·kJ⁻²)	ρ_{ads} (mg/cm³)	n_∞ (cm³/g rock)	K_L (MPa⁻¹)	ρ_{ads} (mg/cm³)
FC-47	40	2.74	0.00731	369	2.73	0.64	385
	60	2.56	0.00731	328	2.52	0.62	344
	80	2.31	0.00731	324	2.34	0.45	337
	100	2.11	0.00731	311	2.17	0.35	326
	120	1.97	0.00731	303	2.11	0.28	303
FC-66	40	4.42	0.00718	415	4.41	0.59	431
	60	4.11	0.00718	406	4.16	0.45	420
	80	3.86	0.00718	396	3.84	0.39	421
	100	3.48	0.00718	377	3.45	0.34	411
	120	3.25	0.00718	348	3.34	0.27	362
FC-72	40	6.01	0.00700	426	5.94	0.63	447
	60	5.56	0.00700	415	5.44	0.51	444
	80	5.25	0.00700	387	5.18	0.42	417
	100	4.87	0.00700	382	4.74	0.36	428
	120	4.36	0.00700	360	4.42	0.28	382

Table 4
Temperature dependency of methane adsorption parameters for the three selected samples in the temperature range of 40–120 °C.

Sample	FC-47	FC-66	FC-72
Adsorption model	3-parameter SDR model		
n_∞ (cm³/g rock)	$-0.010 \times T + 3.136$ ($R^2 = 0.994$)	$-0.015 \times T + 5.013$ ($R^2 = 0.996$)	$-0.020 \times T + 6.810$ ($R^2 = 0.994$)
D (mol²·kJ⁻²)	0.00731	0.00718	0.00700
ρ_{ads} (mg/cm³)	$-0.74 \times T + 385.87$ ($R^2 = 0.85$)	$-0.81 \times T + 453.27$ ($R^2 = 0.93$)	$-0.82 \times T + 459.78$ ($R^2 = 0.994$)
Adsorption model	3-parameter Langmuir model		
n_∞ (cm³/g rock)	$-0.008 \times T + 3.005$ ($R^2 = 0.9587$)	$-0.014 \times T + 4.978$ ($R^2 = 0.980$)	$-0.019 \times T + 6.644$ ($R^2 = 0.9882$)
K_L (MPa⁻¹)	$-0.005 \times T + 0.8715$ ($R^2 = 0.970$)	$-0.0037 \times T + 0.7038$ ($R^2 = 0.9527$)	$-0.0042 \times T + 0.7768$ ($R^2 = 0.9527$)
ρ_{ads} (mg/cm³)	$-0.92 \times T + 412.18$ ($R^2 = 0.92$)	$-0.73 \times T + 467.38$ ($R^2 = 0.73$)	$-0.74 \times T + 482.61$ ($R^2 = 0.78$)

(Stach et al., 1982). In particular, the abundant occurrence of pyrobitumen in our samples indicates that their original organic matter is dominated by oil-prone type I/II kerogens (Leng et al., 2016). According to their size, pyrobitumen particles are further subdivided to connected (>5 μm), wispy (2–5 μm) and speckled (<1–2 μm) pyrobitumen (Cardott et al., 2015). In many cases, speckled bitumen grains and micrinites form a maceral complex, which makes it difficult if not impossible to discriminate them accurately under the resolution of optical microscopy. The random pyrobitumen reflectance values are in the range of 3.2–4.7%, with mean values of 3.7–4.0% (Table 1). Based on the relationship between vitrinite and pyrobitumen reflectance values (Schoenherr et al., 2007), the mean equivalent vitrinite reflectance (EqVRo) values for our samples ranges between 3.8 and 4.1%, reaching the late stage of gas generation.

As shown in Table 1, the relative quartz contents for the eleven samples range from 27.3 to 52.3%; total clays account for 10.5–34.4%; feldspar contents are in the range of 9.1–36.7%, with carbonates varying from below detection limit to 11.9%. All samples contain pyrite, ranging from 3.2 to 4.8%, suggesting a reducing depositional environment. In addition, approximately 13.6% apatite was identified in sample FC-72.

4.2. Specific surface area and pore volume

Typical pore structure parameters are listed in Table 1. The apparent specific surface areas (S_{BET}) for the eleven samples range between 11.1 and 26.2 m²/g rock; the total pore volumes (V_{total}) determined by the adsorbed nitrogen at 77.4 K at a relative pressure of 0.995 range from 8.9 to 18.6 cm³/kg rock whereas the micropore volumes (V_{mic}) by the DR equation with CO_2 adsorption range

between 4.3 and 11.2 cm³/kg, indicating micropore-rich shale samples. While both specific surface area and pore volume are largely positively correlated with TOC (Fig. 4a), their relations to total clay mineral content are complex (Fig. 4b); this implies a predominant control of organic matter on surface area and pore volume, and is also consistent with the results of Ross and Bustin (2009). Based on the relationship between TOC and total surface area (Fig. 4a), the OM specific surface area for our shale samples is estimated to be 148 m²/g TOC, a value that is lower than the value of 228–244 m²/g TOC for the Niutitang Shale samples with lower RqVRo values of 3.12–3.25% (Sun et al., 2015; Li et al., 2016a). This may indicate that the OM methane adsorption capacity would be also reduced since specific surface area can reflect the available adsorption sites for methane in some ways (Gregg and Sing, 1982).

4.3. Methane adsorption at 60 °C

As illustrated in Fig. 5a, the methane excess adsorption (n_{excess}) measured at 60 °C fist increases rapidly and hence shows a declining trend with pressures; the pressures corresponding to the maxima of n_{excess} values (n_{max}^{excess}) for our samples vary less significantly, mostly in the range of 9–12 MPa. According to Eq. (2) or (3), n_{excess} values are expected to be close to zero at very high pressures (Rexer et al., 2013) under which both the adsorbed phase and bulk methane densities are almost the same. At the same time, the n_{max}^{excess} values are largely positively correlated with TOC contents, increasing from 1.34 cm³/g rock for the sample with TOC = 1.8% to 4.10 cm³/g rock for the sample with TOC = 10.7% (Fig. 5b).

Adsorption parameters fitted with the two models mentioned in section 3.4.2 are summarized in Table 2. The fitted values of n_∞ using the 3-parameter SDR model range from 1.80 to 5.84 cm³/g
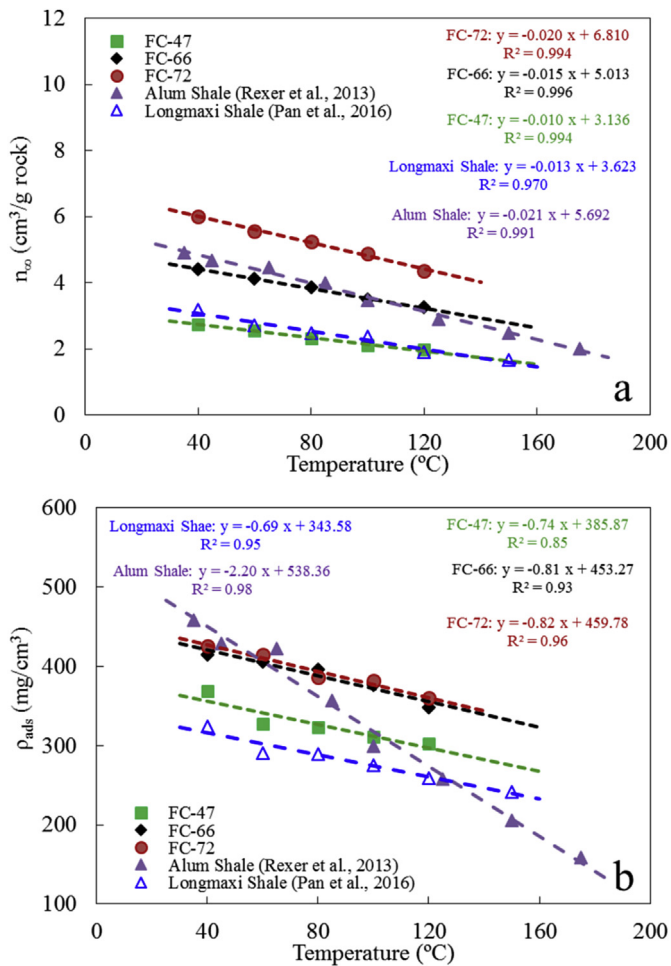
Fig. 7. Plots showing relationships between temperature and maximum methane absolute adsorption capacity (a) and adsorbed phase methane density (b) fitted by the 3-parameter SDR model.

increasing temperatures (Fig. 6). The reduction of n_{max}^{excess} with increasing temperature reflects the exothermic nature of methane adsorption process (Sircar, 1992) and has been confirmed by many other authors (e.g., Rexer et al., 2013; Gasparik et al., 2014a and references therein). Nevertheless, the difference in isotherms may become indistinct at higher pressures (Fig. 6a, c and e); in some cases, the isotherms may intersect with each other and show higher excess sorption at higher temperatures (Gasparik et al., 2015; Tang et al., 2016). Such behaviors are believed to be a result of opposing effects of temperature on isotherm shape-determining Langmuir pressure and bulk methane density (Gasparik et al., 2015) as the Langmuir pressure increases and the bulk methane density decreases with increasing temperature. Therefore, such behaviors of the excess adsorption isotherms at high pressures disappear when measured excess adsorption is plotted against bulk methane density, rather than pressure (Fig. 6b, d and f; Di Giovanni et al., 2001).

The fitted adsorption parameters for the three selected samples are listed in Table 3 and their temperature dependency is summarized in Table 4. It is evident that the two models yield almost the same n_∞ values, though the ρ_{ads} values show some variances (Table 3). The n_∞ values determined with the 3-parameter SDR model are reduced at a rate varying from 0.01 cm^3/g rock/°C for sample FC-47, through 0.015 cm^3/g rock/°C for sample FC-66 to 0.020 cm^3/g rock/°C for sample FC-72, similar to the reduction rates reported by other authors (Fig. 7a). The reduction rate of ρ_{ads} for sample FC-47 is smallest, about 0.74 mg/cm^3/°C; the values for samples FC-66 and FC-72 are similar, approximately 0.81 mg/cm^3/°C and 0.82 mg/cm^3/°C, respectively (Fig. 7b). These values are smaller than the reduction rate of 2.2 mg/cm^3/°C determined for an Alum shale sample (EqVRo ≈ 2.26%, Rexer et al., 2013) but close to the value of 0.7 for a Longmaxi shale sample (EqVRo ≈ 3.0%, Pan et al., 2016). One reason for such a temperature dependence of ρ_{ads} is probably related to the fact that the adsorbed phase is somehow like a liquid phase that would decrease with increasing temperature. Zhou et al. (2000) examined the change of intermolecular distance for adsorbed molecules with temperature, and found that the intermolecular distance between adsorbed molecules would increase with increasing temperature, though such an inter-molecular expansion is smaller than that for the free phase molecules. Considering that the pore volume that may be occupied by adsorbed phase is limited or restricted in a given nanopore (Rexer et al., 2014), it is not a surprise to observe that the maximum methane adsorption capacity (i.e., the product of adsorbed phase density and volume) is also temperature dependent and decreases with increasing temperature. Actually, such a temperature dependency of n_∞ is also observed for coal adsorption (Hildenbrand et al., 2006).

For the 3-parameter Langmuir model, the reduction rates of both n_∞ and ρ_{ads} values with temperature are similar to those determined through the 3-parameter SDR model, ranging from 0.008 to 0.019 cm^3/g rock/°C and from 0.73 to 0.92 mg/cm^3/°C, respectively (Table 4). The reduction rates of K_L values display a range of 0.0037–0.005 MPa^{-1}/°C, with an average value of 0.0043 MPa^{-1}/°C (Table 4). The decreasing trend of K_L values with increasing temperature indicates a higher Langmuir pressure at a higher temperature, and hence a greater desorption capacity (Heller and Zoback, 2014).

4.5. Thermodynamic parameters

Based on the absolute adsorption isotherms reconstructed with the 3-parameter SDR model for the three selected samples, their plots of 1/T_K versus ln(P) were built at specific absolute adsorption quantities that are approximately half of their n_∞ values at 60 °C

rock; the values of ρ_{ads} are in the range of 264–465 mg/cm^3, most of which are smaller than 424 mg/cm^3, i.e., the liquid methane density at its boiling point (Rexer et al., 2013); fitted *D* values range from 0.00621 to 0.00938 and are largely similar to those of other shales (Clarkson and Haghshenas, 2013; Pan et al., 2016; Tian et al., 2016), suggesting methane adsorption on different shales may occur in pores of similar size range, i.e., mainly in micorpores and fine mesopores (Rexer et al., 2014). Fitted n_∞ values for the isotherms at 60 °C using the 3-parameter Langmuir model range from 1.90 to 5.85 cm^3/g rock, quite consistent with the values fitted with 3-parameter SDR model (Table 2); fitted ρ_{ads} values are in the range of 266–541 mg/cm^3, generally greater than the values fitted with the 3-parameter SDR model, and some of them are even remarkably greater than 424 mg/cm^3 (Table 2); fitted K_L values range from 0.40 to 0.68 MPa^{-1}, corresponding to Langmuir pressures of 1.5–2.5 MPa, similar to those of other overmature shales (Wang et al., 2013b; Tian et al., 2016).

4.4. Methane adsorption at different temperatures

To investigate the temperature dependency of methane excess adsorption on shales, isotherms were also measured at multiple temperature for three selected samples with distinct TOC contents. Like the change of n_{excess} with pressure at 60 °C, similar changes are also observed at other temperatures but the n_{max}^{excess} decreases with
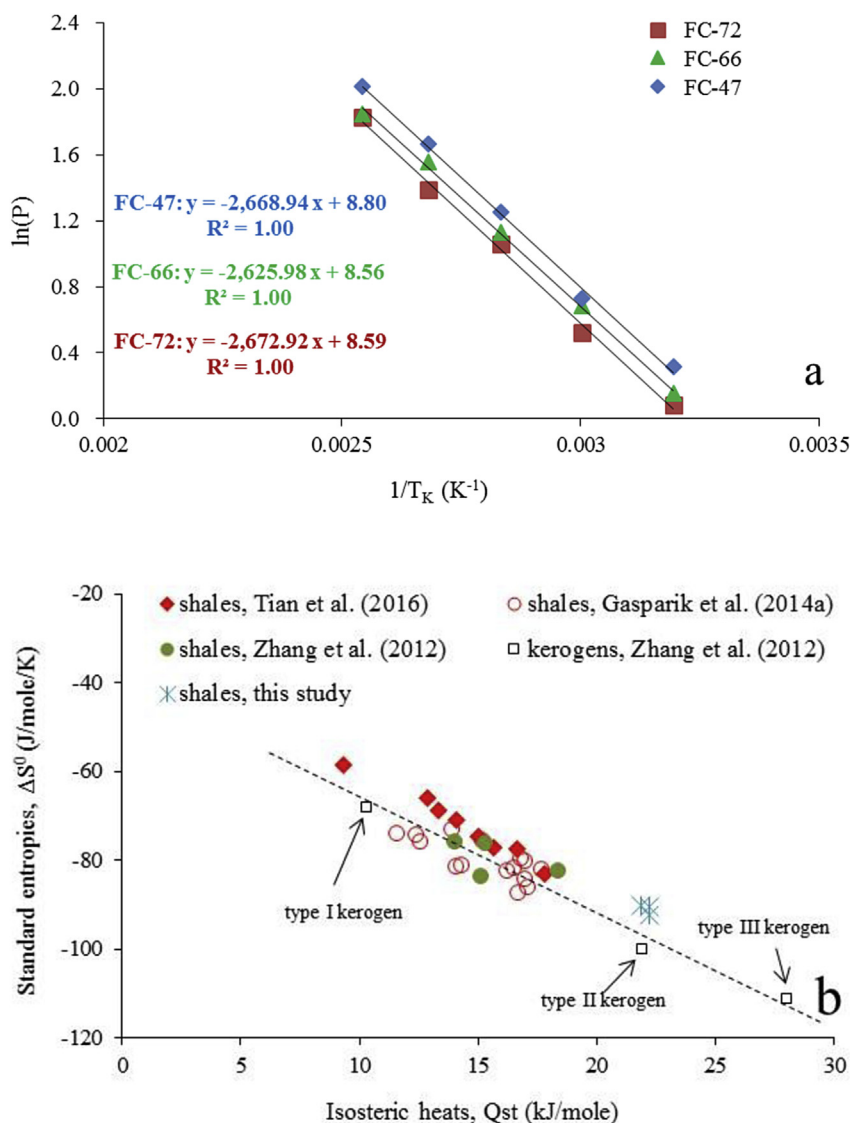
Fig. 8. Plot of ln(P) against $1/T_K$ showing the slopes and intercepts of regressed lines from which isosteric heat and standard entropy are derived, respectively (a), and a comparison of the two parameters for the three selected with those for other shales and kerogens (b).

(Fig. 8a). According to Eq. (4), the isosteric heats (Q_{st}) and adsorption entropies (ΔS^0) were determined from the slopes and intercepts of regression lines, with Q_{st} ranging from 21.8 to 22.2 kJ/mol and ΔS^0 from −90.3 to −92.3 J/mol/K, respectively (Fig. 8b). These values are larger than those reported by other authors for shales with relatively low thermal maturity levels but still fall along the linear line defined by the end members of different kerogens (Fig. 8b; Zhang et al., 2012). Organic matter in our samples is a mixture of type I and II kerogens (Zou et al., 2010), but the thermodynamic parameters are more close to those of type II kerogen (Fig. 8b). Zhang et al. (2012) also found the pore surface of type II kerogen would evolved to that of type III kerogen when the thermal maturation evolved from mature to overmature stage. Mechanism behind such behavior is probably related to the increasing aromaticity of originally more aliphatic organic matter such as type I or II kerogens as a response to elevated thermal maturation (Ross and Bustin, 2009), which would enhance methane affinity to kerogen surface, resulting in large values of both isosteric heat and adsorption entropy (Myers, 2004; Xia et al., 2006).

5. Discussion

5.1. Thermal maturity effect on organic matter adsorption capacity

Like other shales, the maxima of methane absolute adsorption (n_∞) for the Lower Cambrian Niutitang Shale samples at 60 °C are also positively related to TOC content and this relationship is valid in the TOC range of 1.8−11.3% (Fig. 9a); this is because micropores and fine mesopores most favorably form in OM fraction (Ross and Bustin, 2009; Tian et al., 2015), whose methane adsorption potential is much larger than large mesopores or macropores due to larger adsorbed phase density in smaller pores (Mosher et al., 2013). The OM adsorption capacity for different shales could be estimated and compared through normalizing the whole rock adsorption capacity to TOC content only if all shale samples have similar clay mineral types and contents (Gasparik et al., 2014a). Alternatively, it can be represented by the slope value of regression line on the plot of TOC against n_∞ for shale samples with similar EqVRo values (Fig. 9a). For example, the slope value of 0.42 for the
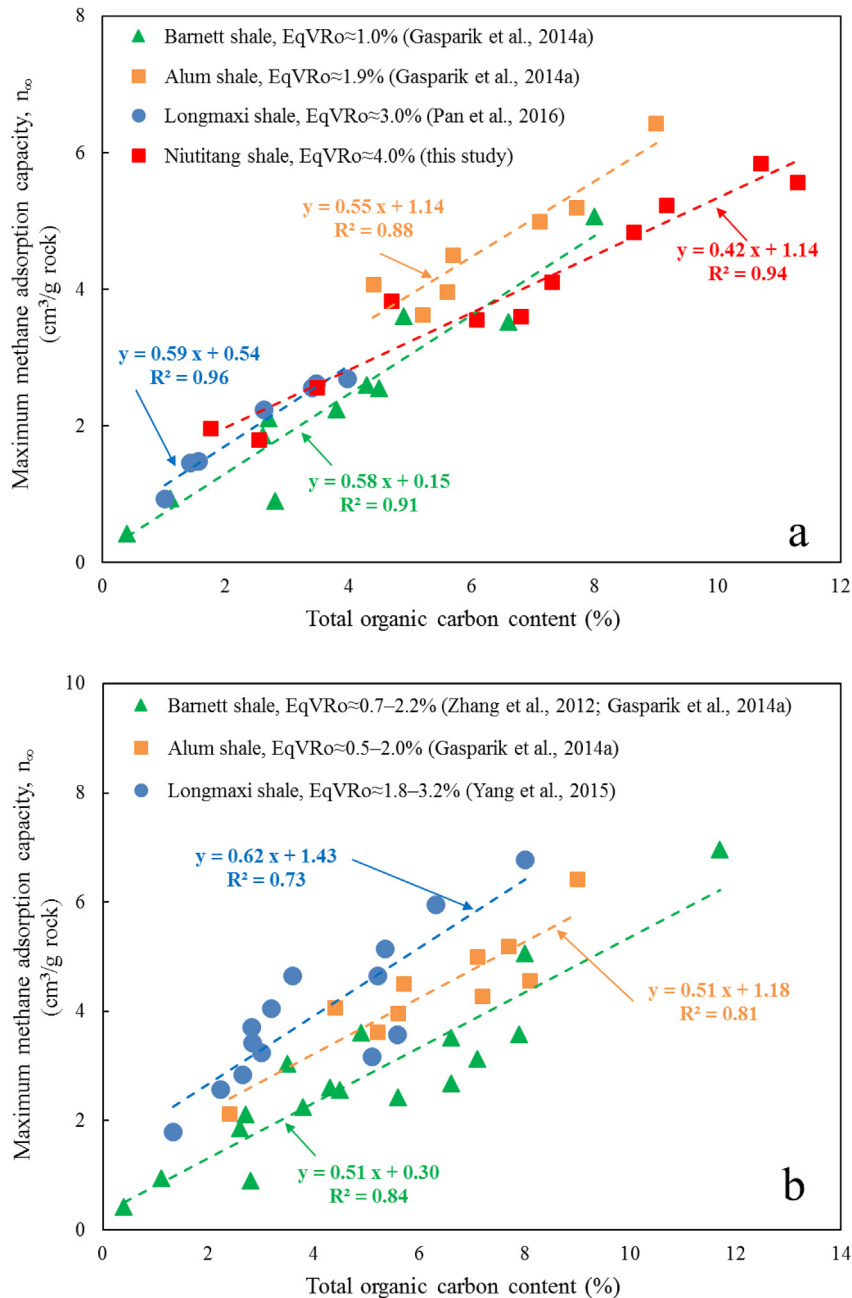
Fig. 9. Plots of maximum methane absolute adsorption capacity (n_∞) with TOC content, showing (a) the adsorption capacity of organic matter in shale samples may be reduced as thermal maturity evolves to EqVRo ≈ 4.0%, and (b) thermal maturity may have only a minor effect on organic matter adsorption capacity for specific sample sets within a wide spectra of thermal maturity levels. The adsorption capacity of organic matter in shales is represented by the slopes of linearly regressed lines.

most mature Niutitang Shale samples represents that the methane adsorption capacity of shales will increase by 0.42 cm³/g rock at each increase of 1% TOC, which suggests the methane adsorption capacity of organic matter is 0.42 cm³/g TOC% or 42 cm³/g TOC at 60 °C, close to the value of 41 cm³/g TOC determined for the Niutitang Shale samples collected from a shallow well close to our study area (Xia et al., 2015). Following this method, the methane adsorption capacities of organic matter in shales are estimated to be 58 cm³/g TOC for the Barnett Shale samples with an approximate EqVRo value of 1.0% at 65 °C, 55 cm³/g TOC for the Alum Shale samples with an approximate EqVRo value of 1.9% at 65 °C, and 59 cm³/g TOC for the Longmaxi Shale samples with an approximate

EqVRo value of 3.0% at 60 °C (Fig. 9a). Considering the above mentioned shales contains similar types of organic matter, i.e., dominantly type I/II marine kerogens (Gasparik et al., 2014b; Pan et al., 2016), the results may imply that at similar temperatures the methane adsorption capacity of organic matter in shales only changes little with thermal maturity in the EqVRo range of 1.0–3.0% but may decline when the thermal maturity evolves to be EqVRo ≈ 4.0%. Nevertheless, this reduction in organic matter adsorption capacity may be compensated by the very enrichment of organic matter in the Niutitang Shale whose TOC values are mostly greater than those of the Lower Silurian Longmaxi Shale (Hao et al., 2013; Li et al., 2016b).
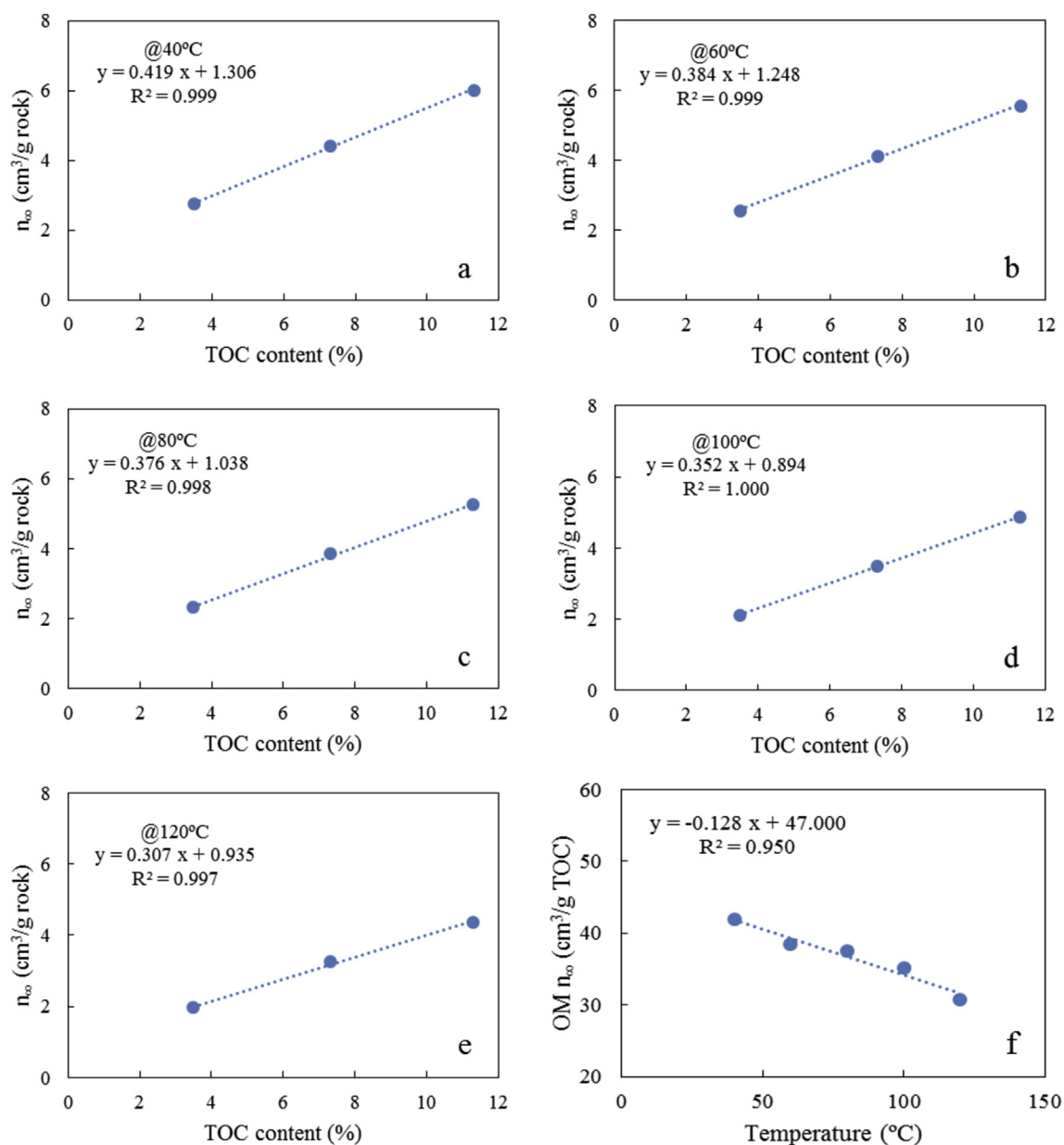
Fig. 10. Plots showing the relationships of fitted maximum methane absolute adsorption capacity (n_∞) with TOC content at different temperatures for the three selected shale samples (a–e) and the temperature-dependency of organic matter adsorption capacity (f).

Actually, a minor thermal maturity effect on OM adsorption was also proposed by Gasparik et al. (2012) who compared the sorption capacities of the immature Mesozoic Posidonia and overmature Paleozoic Geverik samples that are both high in TOC and have similar total clay contents and found no enhancement of sorption capacity. Such phenomenon can be further confirmed by the fairly good linear relationships between TOC and n_∞ for specific sets of shale samples with various EqVRo and TOC content values (Fig. 9b). In terms of the slope values of the regressed lines, the OM adsorption capacities are estimated to be approximately 51 cm³/g TOC for the Alum shales with EqVRo values between 0.5 and 1.9%, 56 cm³/g TOC for the Barnett shales with EqVRo values between 0.7 and 2.2%, and 62 cm³/g TOC for the Longmaxi Shale samples with EqVRo values between 1.8 and 3.2%, all close to the values determined earlier (Fig. 9a). Mechanisms behind such minor thermal

maturity effect of on OM adsorption capacity in the stage of EqVRo = 1.0–3.0% are not completely clear but it may be partly explained by the insignificant variation in micropore volumes within such thermal maturity range (Mastalerz et al., 2013; Hu et al., 2015). As to the reduced OM adsorption capacity at an EqVRo value of 4.0%, which was also observed by Gasparik et al. (2014a), it is probably related to the destruction of micropores in shales at very high thermal maturity levels such as EqVRo > 3.5% (Chen and Xiao, 2014). Nevertheless, this interpretation still needs to be further confirmed in the future through more methane adsorption experiments on kerogens isolated from the Niutitang Shale samples with various thermal maturities, and more details on the evolution of surface area and micropore volume in shales are also required.
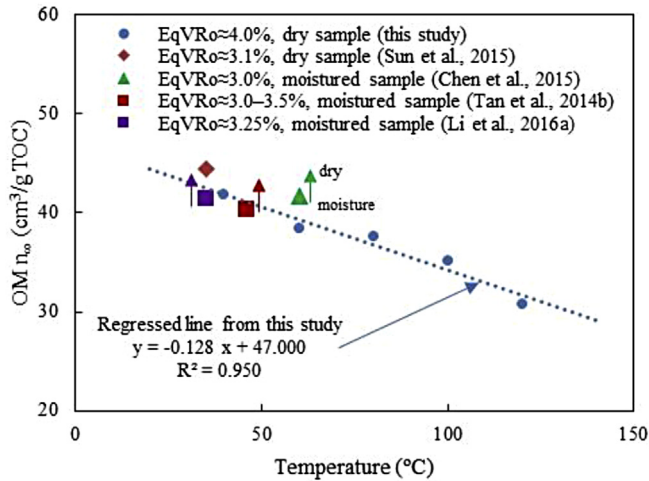
Fig. 11. A comparison plot showing the change of organic matter adsorption capacity (OM n_∞) with temperatures for the Lower Cambrian shales with different thermal maturity levels. The arrows indicate the OM adsorption capacity would be greater when measured in a dry condition.

5.2. Methane adsorption in geological conditions

Methane adsorption in geological conditions can be predicted through the adsorption parameters obtained from experimental results; however, this is only ture when shale reservoirs in sub-surface is as dry as the shale samples used in experiments; otherwise, the predicted methane adsorption would be overestimated (Bruns et al., 2016) because the water in shales may occupy the adsorption sites for methane, and hence lower the total adsorption capacity of a whole rock (Gasparik et al., 2014a and references therein). Based on experimental results, several relationships have been tentatively proposed to correlate mositure content with methane adsorption capacity for wet shales or coals (Levy et al., 1997; Ross and Bustin, 2007); applying these relationships to geological conditions, however, must be cautious because they may change with specific organic/inorganic compositions among shales and simply assume that the equilibrium moisture content experimentally measured at 30 °C represents the real water content in subsurface shales (Ross and Bustin, 2007, 2008). Considering organic matter in shales is more hydrophobic than clay minerals, methane adsorption capacity of organic matter alone could reasonably represent the methane adsorption capacity of a whole rock when it is saturated with water in subsurface (Zhang et al., 2012), though moisture also occur in organic matter when carboxilic functinal groups are present (Nishino, 2001; Chalmers and Bustin, 2007). As our samples contains mainly type I/II kerogens with very high thermal maturity levels, the carboxilic functinal groups may be present in a very low concentration, and therefore the mositure in organic matter is assumed to be minimal.

Based on the n_∞ values fitted with the 3-parameter SDR model at different temperatures for the three selected samples (Table 3), the OM adsorption capacity at specific temperatures ranging from 40 to 120 °C was individually estimated from the slope values of regression lines on the plots of TOC against n_∞ (Fig. 10a–e). It is evident that OM adsorption capacity decreases from 41.9 cm³/g TOC at 40 °C to 30.7 cm³/g TOC at 120 °C, with a reduction rate of approximately 0.128 cm³/g TOC/°C (Fig. 10f). Interestingly, Hildenbrand et al. (2006) also reported a n_∞ reduction rate of approximately 0.1 cm³/g coal/°C for the methane adsorption on coals in the temperature range of 20–170 °C. Fig. 11 further compares the maximum methane absolute adsorption capacity of
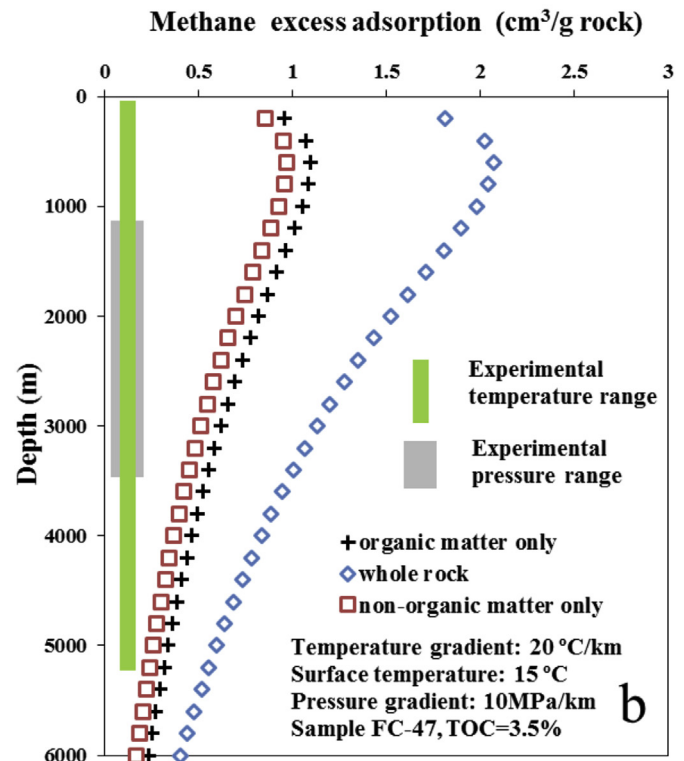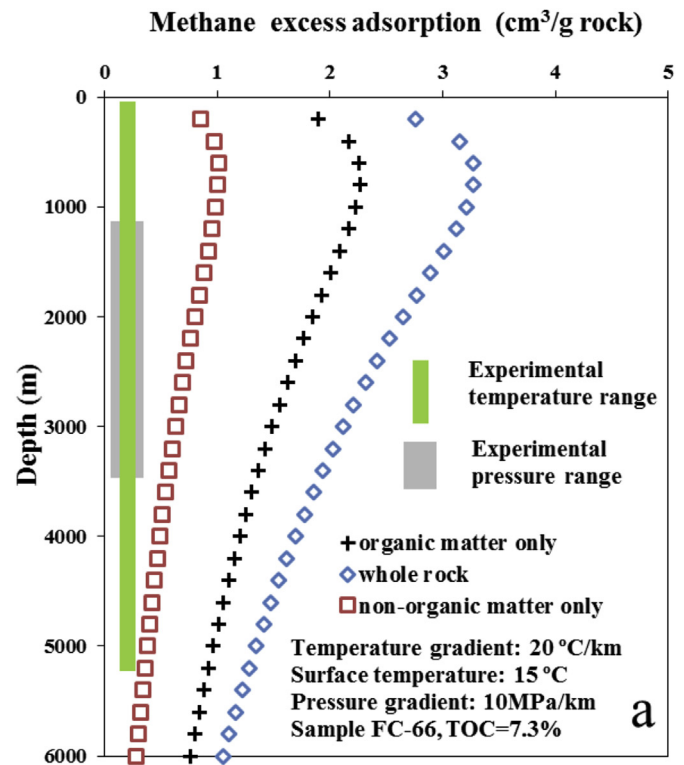

Fig. 12. Changes of methane excess adsorption with burial depth for samples FC-66 (a) and FC-47 (b). The adsorption parameters used here are derived from 3-parameter SDR model (See details in Table 4 and Fig. 10f).

organic matter in the Niutitang Shale samples that have different thermal maturities and were investigated at various temperatures. It is evident that at the same temperature shale samples with a relatively lower thermal maturity would have a greater adsorption capacity if they are all investigated in a dry condition; in some ways this observation supports our previous inference that the OM adsorption capacity may be somehow reduced at very high thermal maturity, and also indicates that the temperature dependence of OM adsorption capacity reported here is reasonable and can be well compared with early results. However, it is worthy to notice that the OM adsorption capacity for our samples is 42.0 cm^3/g TOC when determined from all samples at 60 °C (Fig. 9a), whereas it is about 38.4 cm^3/g TOC in terms of the three selected samples (Fig. 10b), indicating the size of dataset may affect this estimation, and more data are required in the future to achieve such a value as precisely as possible.

The changes of methane excess adsorption with depth were calculated using the 3-parameter SDR model for samples FC-44 and FC-66 that have distinct TOC contents (Fig. 12). The geothermal gradient and ground temperature used for the geological models are 20 °C/km and 15 °C, respectively, and the pressure system is hydrostatic. For whole rock adsorption, the relationships of n_∞ and ρ_{ads} with temperature were listed in Table 4, whereas the pore structure parameter D was assumed to be temperature independent. For OM adsorption, the same relationships as used for whole rock were adopted except a different relationship of n_∞ with temperature as presented in Fig. 10f. The difference between whole rock and organic matter adsorption was presumably interpreted to be the adsorption of non-organic matter (e.g., clays and other minerals). It is evident that the excess adsorption of whole rocks is dominated by OM, though the non-organic matter adsorption has a higher proportion for sample FC-47 that has a lower TOC but higher clay mineral content as compared to sample FC-66. Nevertheless, the non-organic matter adsorption would remarkably diminish for both samples once they are saturated with water in subsurface. Therefore, the real adsorption capacity of a whole shale rock in subsurface might be mainly limited by the enrichment of organic matter that is more hydrophobic than clay minerals (Zhang et al., 2012).

It is also observed that the excess adsorption amount for sample FC-66 (TOC = 7.3%) reaches a maxima at a depth of approximately 800 m, after which it begins to decrease with burial depth and is reduced to be about 1.0 cm^3/g rock at 6000 m for whole rock, with a contribution of 0.76 cm^3/g rock from organic matter and less than 0.30 cm^3/g rock from non-organic matter (Fig. 12a); for sample FC-44 (TOC = 3.5%), the excess adsorption is smaller but similar trend was also observed (Fig. 12b). This diminishing trend suggests the excess adsorption would be negligible when burial depth and temperature are greater enough (Rexer et al., 2013). Once the excess adsorption becomes negligible or to be zero, the gas-in-place (GIP) for a shale system may be mathematically represented by the apparent free gas content calculated in terms of measured or predicted porosity of shales without any adsorption phase volume correction (Ambrose et al., 2012) because the excess adsorption itself has eliminated such a volume (Bruns et al., 2016).

6. Conclusions

Based on geochemical analysis and methane adsorption measurements conducted on eleven Lower Cambrian Niutitang Shale samples, the main conclusions can be summarized as follows:

(1) The Lower Cambrian Niutitang Shale samples investigated here display a wide range of TOC contents, varying from 1.8 to 11.3%; their BET specific surface areas and micropore volumes range from 11.1 to 26.2 m^2/g rock and between 4.3 and 11.2 cm^3/kg rock, respectively, both of which are positively correlated to TOC content; their EqVRo values range from 3.7 to 4.1%, reaching the late stage of gas generation.

(2) Methane maximum absolute adsorption capacity (n_∞) is largely positively correlated with TOC content within a wide TOC range of 1.8–11.3%, which suggests that the TOC control on methane adsorption capacity obtained by other authors for shales with relatively low thermal maturity levels may be extended to a very high thermal maturity level, e.g., EqVRo $\approx$ 4.0%.

(3) Based on our present data and the assumption that thermal maturity effect on methane adsorption capacity is similar for Type I and II kerogens, it is tentatively suggested that thermal maturity might adversely affect methane adsorption capacity of organic matter in shales when it evolves to be EqV-Ro $\approx$ 4.0%; this reduction in OM adsorption capacity, however, may be compensated by the very enrichment of organic matter in the Lower Cambrian Niutitang Shale in our study area.

References

Ambrose, R.J., Hartman, R.C., Diaz-Campos, M., Akkutlu, I.Y., Sondergeld, C.H., 2012. Shale gas-in-place calculations Part I: new pore-scale considerations. SPE J. 17, 219–229.

Bai, D.Y., Jiang, W., Xiong, X., Zhong, X., 2015. Control of tectonic evolution and tectonic framework on the hydrocarbon accumulation in the western side of the Xuefeng Mountain. Geol. Mineral Resour. South China 31, 199–209 (in Chinese with English abstract).

Bruns, B., Littke, R., Gasparik, M., van Wees, J.-D., Nelskamp, S., 2016. Thermal evolution and shale gas potential estimation of the Wealden and Posidonia Shale in NW-Germany and The Netherlands: a 3D basin modelling study. Basin Res. 28, 2–33.

Cardott, B.J., Landis, C.R., Curtis, M.E., 2015. Post-oil solid bitumen network in the Woodford Shale, USA— a potential primary migration pathway. Int. J. Coal Geol. 139, 106–113.

Chalmers, G.R.L., Bustin, R.M., 2007. The organic matter distribution and methane capacity of the Lower Cretaceous strata of northeastern British Columbia, Canada. Int. J. Coal Geol. 70, 223–339.

Chalmers, G.R.L., Bustin, R.M., 2008. Lower Cretaceous gas shales in northeastern British Columbia, Part I: geological controls on methane sorption capacity. Bull. Can. Petrol. Geol. 56, 1–21.

Chen, F., Lu, S., Ding, X., 2015. Evaluation model of gas adsorption capacity of shale: a case study of adsorbed gas content from Niutitang Formation in Qiannan Depression. J. China Univ. Min. Tech. 44, 508–513 (in Chinese with English abstract).

Chen, J., Xiao, M., 2014. Evolution of nanoporosity in organic-rich shales during thermal maturation. Fuel 129, 173–181.

Chen, S., Zhu, Y., Wang, H., Liu, H., Wei, W., Fang, J., 2011. Shale gas reservoir characterization: a typical case in the southern Sichuan Basin of China. Energy 36, 6609–6616.

Clarkson, C.R., Haghshenas, B., 2013. Modeling of Supercritical Fluid Adsorption on Organic-rich Shales and Coal. Society of Petroleum Engineers. Paper No. SPE 164532, 24 pp.

Curtis, J.B., 2002. Fractured shale-gas systems. Am. Assoc. Petrol. Geol. Bull. 86, 1921–1938.

Dai, J., Zou, C., Dong, D., Ni, Y., Wu, W., Gong, D., Wang, Y., Huang, S., Huang, J., Fang, C., Liu, D., 2016. Geochemical characteristics of marine and terrestrial shale gas in China. Mar. Petrol. Geol. 76, 444–463.

De Weireld, G., Frère, M., Jadot, R., 1999. Automated determination of high-temperature and high-pressure gas adsorption isotherms using a magnetic suspension balance. Meas. Sci. Technol. 10, 117–126.

Di Giovanni, O., Dörfler, W., Mazzotti, M., Morbidelli, M., 2001. Adsorption of supercritical carbon dioxide on silica. Langmuir 17, 4316—4321.

Gasparik, M., Bertier, P., Gensterblum, Y., Ghanizadeh, A., Krooss, B.M., Littke, R., 2014a. Geological controls on the methane storage capacity in organic-rich shales. Int. J. Coal Geol. 123, 34—51.

Gasparik, M., Gensterblum, Y., Ghanizadeh, A., Weniger, P., Krooss, B.M., 2015. High-pressure/high-temperature methane-sorption measurements on carbonaceous shales by the manometric method: experimental and data-evaluation considerations for improved accuracy. SPE J. 20, 790—809.

Gasparik, M., Ghanizadeh, A., Bertier, P., Gensterblum, Y., Bouw, S., Krooss, B.M., 2012. High-pressure methane sorption isotherms of black shales from The Netherlands. Energy & Fuels 26, 4995—5004.

Gasparik, M., Rexer, T.F.T., Aplin, A.C., Billemont, P., DeWeireld, G., Gensterblum, Y., Henry, M., Krooss, B.M., Liu, S., Ma, X., Sakurovs, R., Song, Z., Staib, G., Thomas, K.M., Wang, S., Zhang, T., 2014b. First international inter-laboratory comparison of high-pressure CH4, CO2 and C2H6 sorption isotherms on carbonaceous shales. Int. J. Coal Geol. 132, 131—146.

Gensterblum, Y., Merkel, A., Busch, A., Krooss, B.M., 2013. High-pressure CH4 and CO2 sorption isotherms as a function of coal maturity and the influence of moisture. Int. J. Coal Geol. 118, 45—57.

Gregg, S.J., Sing, K.S.W., 1982. Adsorption, Surface Area, and Porosity. Academic Press, New York, 303 pp.

Han, S., Zhang, J., Li, Y., Horsfield, B., Tang, X., Jiang, W., Chen, Q., 2013. Evaluation of lower cambrian shale in northern Guizhou Province, south China: implications for shale gas potential. Energy & Fuels 27, 2933—2941.

Hao, F., Zou, H., Lu, Y., 2013. Mechanisms of shale gas storage: implications for shale gas exploration in China. Am. Assoc. Petrol. Geol. Bull. 97, 1325—1346.

Heller, R., Zoback, M., 2014. Adsorption of methane and carbon dioxide on gas shale and pure mineral samples. J. Unconv. Oil Gas Resour. 8, 14—24.

Hildenbrand, A., Krooss, B.M., Busch, A., Gaschnitz, R., 2006. Evolution of methane sorption capacity of coal seams as a function of burial history—a case study from the Campine Basin, NE Belgium. Int. J. Coal Geol. 66, 179—203.

Hu, H., Zhang, T., Wiggins-Camacho, J.D., Ellis, G.S., Lewan, M.D., Zhang, X., 2015. Experimental investigation of changes in methane adsorption of bitumen-free Woodford Shale with thermal maturation induced by hydrous pyrolysis. Mar. Petrol. Geol. 59, 114—128.

Jarvie, D.M., 2012. Shale resource systems for oil and gas: Part 1—shale-gas resource systems. In: Breyer, J.A. (Ed.), Shale Reservoirs—Giant Resources for the 21st Century, vol. 97. AAPG Memoir, pp. 69—87.

Ji, L., Zhang, T., Milliken, K.L., Qu, J., Zhang, X., 2012. Experimental investigation of main controls to methane adsorption in clay-rich rocks. Appl. Geochem. 27, 2533—2545.

Jin, Z., Firoozabadi, A., 2014. Effect of water on methane and carbon dioxide sorption in clayminerals by Monte Carlo simulations. Fluid Phase Equil. 382, 10—20.

Krooss, B.M., van Bergen, F., Gensterblum, Y., Siemons, N., Pagnier, H.J.M., David, P., 2002. High pressure CH4 and carbon dioxide adsorption on dry and moisture equilibrated Pennsylvanian coals. Int. J. Coal Geol. 51, 69—92.

Leng, J., Gong, D., Li, F., Li, P., 2016. Analysis of the shale gas exploration prospect of the Niutitang Formation in northeastern Guizhou area. Earth Sci. Front. 23, 29—38 (in Chinese with English abstract).

Levy, J.H., Day, S.J., Killingley, J.S., 1997. Methane capacities of Bowen Basin coals related to coal properties. Fuel 76 (9), 813—819.

Li, A., Ding, W., He, J., Dai, P., Yin, S., Xie, F., 2016a. Investigation of pore structure and fractal characteristics of organic rich shale reservoirs: a case study of Lower Cambrian Qiongzhusi formation in Malong block of eastern Yunnan Province, South China. Mar. Petrol. Geol. 70, 46—57.

Li, X., Shen, Z., Li, W., Huang, H., 2016b. Exploration and development potential of Niutitang Fm shale gas in Fenggang area, North Guizhou. Nat. Gas. Ind. 36, 72—79.

Liu, L., Li, S., Dai, L., Suo, Y., Liu, B., Zhang, G., Wang, Y., Liu, E., 2012. Geometry and timing of mesozoic deformation in the western part of the xuefeng tectonic belt, south China: implications for intra-continental deformation. J. Asian Earth Sci. 49, 330—338.

Liu, Z., Gao, B., Zhang, Y., Du, W., Feng, D., Nie, H., 2017. Types and distribution of the shale sedimentary facies of the lower cambrian in upper yangtze area, south China. Petrol. Explor. Dev. 44, 1—11.

Ma, Y., Zhong, N., Li, D., Pan, Z., Cheng, L., Liu, K., 2015. Organic matter/clay mineral intergranular pores in the Lower Cambrian Lujiaping Shale in the north-eastern part of the upper Yangtze area, China: a possible microscopic mechanism for gas preservation. Int. J. Coal Geol. 137, 38—54.

Mastalerz, M., Schimmelmann, A., Drobniak, A., Chen, Y., 2013. Porosity of Devonian and Mississippian New Albany Shale across a maturation gradient: insights from organic petrology, gas adsorption, and mercury intrusion. AAPG Bull. 97, 1621—1643.

Mohammad, S.A., Sudibandriyo, M., Fitzgerald, J.E., Liang, X., Robinson Jr., R.L., Gasem, K.A.M., 2012. Measurements and modeling of excess adsorption of pure and mixed gases on wet coals. Energy Fuels 26, 2899—2910.

Mosher, K., He, J., Liu, Y., Rupp, E., Wilcox, J., 2013. Molecular simulation of methane adsorption in micro- and mesoporous carbons with applications to coal and gas shale systems. Int. J. Coal Geol. 109—110, 36—44.

Myers, A.L., 2004. Characterization of nanopores by standard enthalpy and entropy of adsorption of probe molecules. Colloids Surfaces A Physicochem. Eng. Aspect 241, 9—14.

Myers, A.L., Monson, P.A., 2002. Adsorption in porous materials at high pressure: theory and experiment. Langmuir 18, 10261—10273.

Nie, H., Zhang, J., Li, Y., 2011. Accumulation conditions of the lower cambrian shale gas in the Sichuan Basin and its periphery. Acta Pet. Sin. 32, 959—967 (in Chinese with English abstract).

Nishino, J., 2001. Adsorption of water vapour and carbon dioxide at carboxylic functional groups on the surface of coal. Fuel 80, 757—764.

Ottiger, S., Pini, R., Storti, G., Mazzotti, M., 2008. Competitive adsorption equilibria of CO2 and CH4 on a dry coal. Adsorption 14, 539—556.

Pan, L., Xiao, X.M., Tian, H., Zhou, Q., Cheng, P., 2016. Geological models of gas in place of the Longmaxi shale in Southeast Chongqing, south China. Mar. Petrol. Geol. 73, 433—444.

Pepper, A.S., Dodd, T.A., 1995. Simple kinetic models of petroleum formation. Part II: oil-gas cracking. Mar. Petrol. Geol. 12, 321—340.

Rexer, T.F., Mathia, E.J., Aplin, A.C., Thomas, K.M., 2014. High-pressure methane adsorption and characterization of pores in Posidonia shales and isolated kerogens. Energy & Fuels 28, 2886—2901.

Rexer, T.F.T., Benham, M.J., Aplin, A.C., Thomas, K.M., 2013. Methane adsorption on shale under simulated geological temperature and pressure conditions. Energy & Fuels 27, 3099—3109.

Ross, D.J.K., Bustin, R.M., 2007. Shale gas potential of the lower jurassic gordondale member, northeastern british columbia, Canada. Bull. Can. Petrol. Geol. 55, 51—75.

Ross, D.J.K., Bustin, R.M., 2008. Characterizing the shale gas resource potential of Devonian—Mississippian strata in the Western Canada sedimentary basin: application of an integrated formation evaluation. AAPG Bull. 92, 87—125.

Ross, D.J.K., Bustin, R.M., 2009. The importance of shale composition and pore structure upon gas storage potential of shale gas reservoirs. Mar. Petrol. Geol. 26, 916—927.

Rouquerol, J., Llewellyn, P., Rouquerol, F., 2007. Is the BET equation applicable to microporous adsorbents? Stud. Surf. Sci. Catal. 160, 49—56.

Schoenherr, J., Littke, R., Urai, J.L., Kukla, P.A., Rawahi, Z., 2007. Polyphase thermal evolution in the Infra-Cambrian Ara group (South Oman salt basin) as deduced by maturity of solid reservoir bitumen. Org. Geochem. 38, 1293—1318.

Sircar, S., 1992. Estimation of isosteric heats of adsorption of single gas and multicomponent gas mixtures. Ind. Eng. Chem. Res. 31, 1813—1819.

Stach, E., Mackowsky, M.-T., Teichmüller, M., Taylor, G.H., Chandra, D., Teichmüller, R., 1982. Stach's Textbook of Coal Petrology. Gebrüder Borntraeger, Stuttgart.

Su, W., Li, Z., Ettensohn, F.R., Johnson, M.E., Huff, W.D., Wang, W., Ma, C., Li, L., Zhang, L., Zhao, H., 2007. Distribution of black shale in the wufeng-longmaxi formations (Ordovician-Silurian), south China: major control ling factors and implications. Earth Sci. —J. China Univ. Geosci. 32, 819—827 (in Chinese with English abstract).

Sun, M., Yu, B., Chen, S., Xia, W., Ye, R., 2015. Reservoir characteristics and adsorption capacity of the Lower Cambrian Niutitang Formation shale in the southeast of Chongqing: a case study of well Yuke 1 and well Youke 1. J. Northeast Petrol. Univ. 39, 69—79 (in Chinese with English abstract).

Tan, J., Weniger, P., Krooss, B.K., Merkel, A., Horsfield, B., Zhang, J., Boreham, C.J., van Graas, G., Tocher, B.A., 2014a. Shale gas potential of the major marine shale formations in the Upper Yangtze Platform, South China, Part II: methane sorption capacity. Fuel 129, 204—218.

Tan, J., Horsfield, B., Fink, R., Krooss, B., Schulz, H.-M., Rybacki, E., Zhang, J., Boreham, C.J., van Graas, G., Tocher, B.A., 2014b. Shale gas potential of the major marine shale formations in the Upper Yangtze Platform, South China, Part III: mineralogical, lithofacial, petrophysical, and rock mechanical properties. Energy & Fuels 28, 2322—2342.

Tang, X., Ripepi, N., Stadie, N.P., Yu, L., Hall, M.R., 2016. A dual-site Langmuir equation for accurate estimation of high pressure deep shale gas resources. Fuel 185, 10—17.

Tian, H., Guo, T., Hu, D., Tang, L., Wo, Y., Song, L., Yang, Z., 2006. Marine lower assemblage and exploration prospect of central Guizhou Uplift and its adjacent areas. J. Palaeogeogr. 8, 509—518 (in Chinese with English abstract).

Tian, H., Li, T., Zhang, T., Xiao, X., 2016. Characterization of methane adsorption on overmature Lower Silurian—Upper Ordovician shales in Sichuan Basin, southwest China: experimental results and geological implications. Int. J. Coal Geol. 156, 36—49.

Tian, H., Pan, L., Xiao, X.M., Wilkins, R.W.T., Meng, Z.P., Huang, B.J., 2013. A preliminary study on the pore characterization of Lower Silurian black shales in the Chuandong Thrust Fold Belt, Southwestern China using low pressure N2 adsorption and FE-SEM methods. Mar. Petrol. Geol. 48, 8—19.

Tian, H., Pan, L., Zhang, T., Xiao, X., Meng, Z., Huang, B., 2015. Pore characterization of organic-rich lower cambrian shales in qiannan depression of Guizhou Province, southwestern China. Mar. Petrol. Geol. 62, 28—43.

Wang, F.P., Reed, R.M., John, A., Katherine, G., 2009. Pore Networks and Fluid Flow in Gas Shales. SPE 124253.

Wang, F., Guan, J., Feng, W., Bao, L., 2013a. Evolution of overmature marine shale porosity and implication to the free gas volume. Petrol. Explor. Dev. 40, 819—824.

Wang, S., Song, Z., Cao, T., Song, X., 2013b. The Methane Sorption Capacity of Paleozoic Shales from the Sichuan Basin, China. Mar. Petrol. Geol. 44, 112—119.

Wang, Y., Leng, J., Li, P., Li, F., 2016. Characteristics and its main enrichment controlling factors of shale gas of the Lower Cambrian Niutitang Formation in northeastern Guizhou Province. J. Palaeogeogr. 18, 605—614 (in Chinese with English abstract).

Wang, Z., Xie, Y., Yang, P., Zhuo, J., He, J., Xie, S., 2012. Marine basin evolution and oil and gas geology of Sinian-early Paleozoic period on the western side of the

Xuefeng Mountain. Geol. Bull. China 31, 1795–1811 (in Chinese with English abstract).

Weniger, P., Kalkreuth, W., Busch, A., Krooss, B.M., 2010. High-pressure methane and carbon dioxide sorption on coal and shale samples from the Paraná Basin, Brazil. Int. J. Coal Geol. 84, 190–205.

Wu, Z., Zuo, Y., Wang, S., Chen, J., Wang, A., Liu, L., Xu, Y., Sunwen, J., Cao, J., Yu, M., Lu, C., Wu, Y., 2017. Numerical study of multi-period palaeotectonic stress fields in Lower Cambrian shale reservoirs and the prediction of fractures distribution: a case study of the Niutitang Formation in Feng'gang No. 3 block, South China. Mar. Petrol. Geol. 80, 369–381.

Xia, J., Wang, S., Cao, T., Yang, J., Song, Z., 2015. The characteristics of pore structure and its gas storage capacity of the Lower Cambrian shales from the northern Guizhou Province. Nat. Gas. Geosci. 26, 1744–1754 (in Chinese with English abstract).

Xia, X., Litvinov, S., Muhler, M., 2006. A consistent approach to adsorption thermodynamics on heterogeneous surfaces using different empirical energy distribution model. Langmuir 22, 8063–8070.

Yang, F., Ning, Z., Wang, Q., Liu, H., 2016. Pore structure of Cambrian shales from the Sichuan Basin in China and implications to gas storage. Mar. Petrol. Geol. 70, 14–26.

Yang, F., Ning, Z., Zhang, R., Zhao, H., Krooss, B.M., 2015. Investigations on the methane sorption capacity of marine shales from Sichuan Basin, China. Int. J. Coal Geol. 146, 104–117.

Zhang, T.W., Ellis, G.S., Rupple, S.C., Milliken, K., Yang, R., 2012. Effect of organic matter type and thermal maturity on methane adsorption in shale-gas systems. Org. Geochem. 47, 120–131.

Zhou, W., Jin, W.H., Xie, R.C., Chen, W.L., Qiu, D.Z., 2012. An analysis of geological characteristics and destruction types of hydrocarbon accumulation in the basin-mountain transitional zone on the western side of the Xuefeng Mountain. Geol. Bull. China 31, 1838–1851 (in Chinese with English abstract).

Zhou, L., Zhou, Y., Li, M., Chen, P., Wang, Y., 2000. Experimental and modeling study of the adsorption of supercritical methane on a high surface activated carbon. Langmuir 16, 5955–5959.

Zou, C., Dong, D., Wang, S., Li, J., Li, X., Wang, Y., Li, D., Cheng, K., 2010. Geological characteristics and resource potential of shale gas in China. Petrol. Explor. Dev. 37, 641–653.